Molecular Therapy
Original Article

Improved Noninvasive *In Vivo* Tracking of AAV-9 Gene Therapy Using the Perchlorate-Resistant Sodium Iodide Symporter from Minke Whale

Susanna C. Concilio,[1,2] Lukkana Suksanpaisan,[3] Linh Pham,[1] Kah-Whye Peng,[1,3] and Stephen J. Russell[1,3]

[1]Department of Molecular Medicine, Mayo Clinic, Rochester, MN 55905, USA; [2]Mayo Clinic Graduate School of Biomedical Sciences, Mayo Clinic, Rochester, MN 55905, USA; [3]Imanis Life Sciences, LLC, Rochester, MN 55901, USA

The sodium iodide symporter (NIS) is widely used as a reporter gene to noninvasively monitor the biodistribution and durability of vector-mediated gene expression via gamma scintigraphy, single-photon emission computed tomography (SPECT), and positron-emission tomography (PET). However, the approach is limited by background signal due to radiotracer uptake by endogenous NIS-expressing tissues. In this study, using the SPECT tracer pertechnetate ($^{99m}TcO_4$) and the PET tracer tetrafluoroborate ($B^{18}F_4$), in combination with the NIS inhibitor perchlorate, we compared the transport properties of human NIS and minke whale (*Balaenoptera acutorostrata scammoni*) NIS *in vitro* and *in vivo*. Based on its relative resistance to perchlorate, the NIS protein from minke whale appeared to be the superior candidate reporter gene. SPECT and PET imaging studies in nude mice challenged with NIS-encoding adeno-associated virus (AAV)-9 vectors confirmed that minke whale NIS, in contrast to human and endogenous mouse NIS, continues to function as a reliable reporter even when background radiotracer uptake by endogenous NIS is blocked by perchlorate.

INTRODUCTION

Non-invasive *in vivo* imaging of viral vectors and cell carriers is essential to both preclinical and clinical studies. Determining biodistribution, gene expression, replication, spread, and durability are critical to understanding and improving treatments. Anatomical imaging such as X-ray, computed tomography (CT), and some types of magnetic resonance imaging (MRI) typically provide little information regarding these cell-level processes. The emergence of several molecular imaging modalities, such as optical imaging, single photon emission CT (SPECT), and positron emission tomography (PET) during the last several decades, has improved the precision with which certain molecular processes can be followed. Biological specificity can be determined either by the imaging compound or by a transgene.

One such transgene is the sodium iodide symporter (NIS). NIS, encoded by the gene *SLC5A5* in humans, mediates the concentration of iodide into the thyroid gland for thyroid hormonogenesis. NIS is expressed in other tissues, such as lactating breast, stomach, intestine, salivary glands, kidney, ovary, testes, and the choroid plexus in the brain.[1–7] Human NIS exists primarily as a dimer of a 643-residue multi-N-linked-glycosylated protein with 13 putative α-helical transmembrane domains, with an extracellular N terminus and intracellular C terminus.[8–11] NIS exclusively transports monovalent anions, with a wide range of substrates, including iodide (I^-), tetrafluoroborate (BF_4^-), pertechnetate (TcO_4^-), thiocyanate (SCN^-), and the potent competitive substrate perchlorate (ClO_4^-), which is commonly referred to as a NIS inhibitor.[12,13]

NIS provides the following advantages over other commonly used imaging and therapeutic transgenes: (1) NIS is a self-protein in chordate animals, which reduces the risk of an immune response against transfected or transduced tissues, and many species of NIS protein are sequenced and cloned, expanding the utility of NIS to various model organisms. (2) NIS transports carrier-free radiotracers useful for several imaging modalities, including ^{123}I, ^{125}I, ^{131}I, $^{99m}TcO_4$, and $^{188}ReO_4$ for SPECT, ^{124}I and ^{18}F-BF_4 for PET, and ^{131}I for optical imaging via Cherenkov luminescence.[14,15] (3) NIS can deliver targeted radiation to malignant tissues by concentrating the beta-emitting radioisotopes ^{131}I, $^{186}ReO_4$, $^{188}ReO_4$, and alpha-emitting ^{211}At.[16–18] Due to these desirable attributes, NIS has been used in many applications, such as tracking viral infection, replication, and spread in oncolytic virotherapy in animals and humans, tracking the intensity and durability of gene and cell therapies, and for treatment of NIS-expressing tumors with radioisotopes.[14,19–36]

Despite the growing utility of NIS as a reporter gene, there remain several challenges to NIS imaging and therapy. Endogenous NIS expression, efflux of radiotracer from NIS-expressing cells, and suboptimal NIS expression in target tissues decrease the efficacy of NIS imaging. The greatest problem lies with endogenous NIS expression. Concentrations of radioisotopes in non-target tissues that naturally express NIS, such as the thyroid, salivary glands, and stomach, reduce

Received 4 August 2020; accepted 25 September 2020;
https://doi.org/10.1016/j.ymthe.2020.09.036.

Correspondence: Stephen J. Russell, Department of Molecular Medicine, Mayo Clinic, Rochester, MN 55905, USA.
E-mail: sjr@mayo.edu

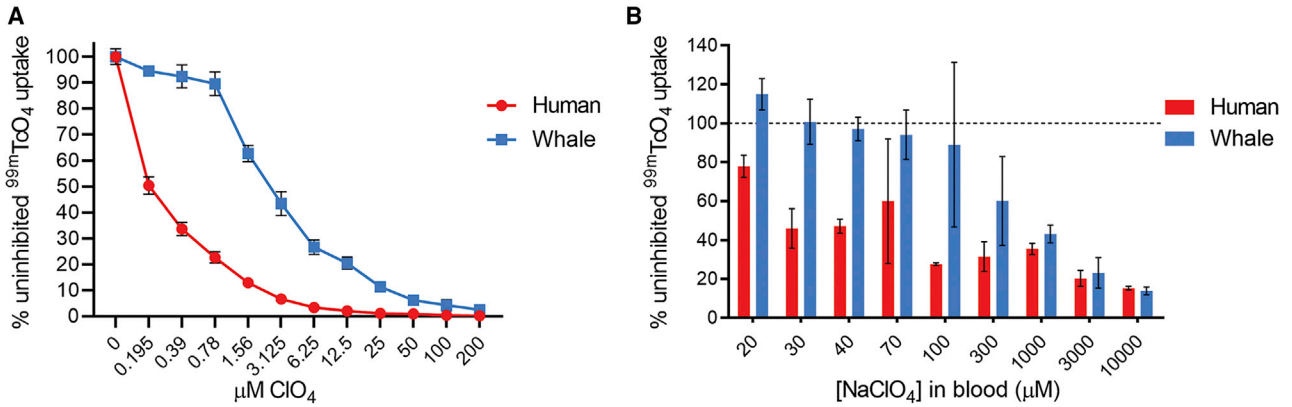

Figure 1. Perchlorate Dose-Response Assays with Pertechnetate *In Vitro* and *In Vivo*

(A) Perchlorate inhibition of $^{99m}TcO_4$ uptake in lentivirally transduced HeLa cells. (B) Perchlorate inhibition of $^{99m}TcO_4$ uptake in the livers of mice transduced with AAV-9-CAG-human NIS or AAV-9-CAG-minke whale NIS. Values in (A) are averages of duplicate assays with standard deviation. Values in (B) represent average values of two mice.

the specificity and resolution of NIS imaging. This uptake also limits the safety of NIS radiotherapy: due to the sensitivity of the thyroid to radioactive iodine, the only approved uses of ^{131}I are for differentiated thyroid cancer and hyperthyroidism.[37] The broader application of NIS-related therapy in other cancers following NIS gene transfer will therefore remain nonviable unless a strategy is developed to prevent collateral destruction of the thyroid gland, which sentences the patient to lifelong thyroid hormone replacement therapy. Moreover, the use of ^{131}I in both preclinical and clinical applications is not without substantial side effects in the salivary glands, lacrimal glands, testes, uterus, and gastrointestinal tract.[38–42] A recent report by the National Cancer Institute correlated treatment with ^{131}I for hyperthyroidism with an increased risk of several solid cancers, especially breast cancer.[43] The thyroid and salivary glands are especially sensitive to NIS-mediated radioisotope uptake and limit the practical application of NIS imaging and treatment.

Several studies have explored ways to improve NIS-based imaging and therapy. ^{131}I therapy with rat NIS required a lower dose for cancer therapy compared to human NIS.[44] Rat NIS concentrated more radiotracer in transplanted bone mesenchymal stem cells versus human NIS.[45] The use of the oral contrast agent barium sulfate was able to define the stomach in SPECT/CT imaging and block some of the gamma ray emissions from radioisotope collected in the stomach.[46] Codon optimization of NIS led to a protein with 2.3-fold greater uptake activity than the human cDNA.[47] However, none of these approaches prevent uptake of radiotracer by endogenous NIS, which remains the most significant barrier to safe and effective NIS imaging and treatment.

A possible solution to this obstacle is perchlorate inhibition. Perchlorate is an effective inhibitor of NIS-mediated radioisotope concentration *in vitro* and *in vivo*, and it is already US Food and Drug Administration (FDA) approved (as Perchloracap).[45,48] Use of a perchlorate-resistant NIS protein would enable inhibition of endogenous NIS while maintaining utility. A previous study by our group identified the NIS protein from minke whale (*Balaenoptera acutorostrata scammoni*) to be partially resistant to perchlorate inhibition of NIS-mediated radioisotope uptake.[49] In the present study, we investigated whether this enhanced perchlorate resistance could be exploited by using perchlorate to decrease radioisotope uptake in tissues expressing endogenous mouse NIS but not in tissues transduced with adeno-associated virus (AAV-9) vectors expressing minke whale NIS.

RESULTS

In Vitro and *In Vivo* Perchlorate Dose-Response Assays

To determine the sensitivity of human NIS (hNIS) and minke whale NIS (wNIS) to perchlorate, perchlorate dose-response assays were performed *in vitro* and *in vivo* using $^{99m}TcO_4$ as the NIS radiotracer. Puromycin-selected HeLa cells transduced with hemagglutinin (HA)-tagged NIS-expressing lentiviral vectors were used for the *in vitro* experiments. Flow cytometry characterization of hNIS- and wNIS-expressing cells is provided in Figure S1. hNIS-expressing cells were much more sensitive to perchlorate inhibition of $^{99m}TcO_4$ uptake than were cells expressing wNIS, with half-maximal inhibitory concentration (IC_{50}) values of 0.1948 and 2.858 μM in hNIS and wNIS, respectively (Figure 1A). An *in vivo* dose-response assay was performed to determine the appropriate concentration of perchlorate to use for the comparative imaging studies. Mice infected with 3×10^{12} viral particles (vp)/kg of either AAV-9-CAG-hNIS (CAG, cytomegalovirus [CMV] early enhancer/chicken β-actin promoter) or AAV-9-CAG-wNIS were subjected to serial SPECT/CT imaging on different days after pretreatment with increasing concentrations of perchlorate administered prior to $^{99m}TcO_4$ injection. An estimated blood concentration of 100 μM was selected as resulting in the widest gap between the hNIS and wNIS signal while maintaining sufficient radiotracer uptake in the transduced liver (Figure 1B).

SPECT/CT Imaging with $^{99m}TcO_4$ and Perchlorate

Mice infected with either 3×10^{12} vp/kg AAV-9-CAG-hNIS or AAV-9-CAG-wNIS were capable of concentrating $^{99m}TcO_4$ in both AAV-9-tranduced tissues (heart, liver, and brown adipose) and in

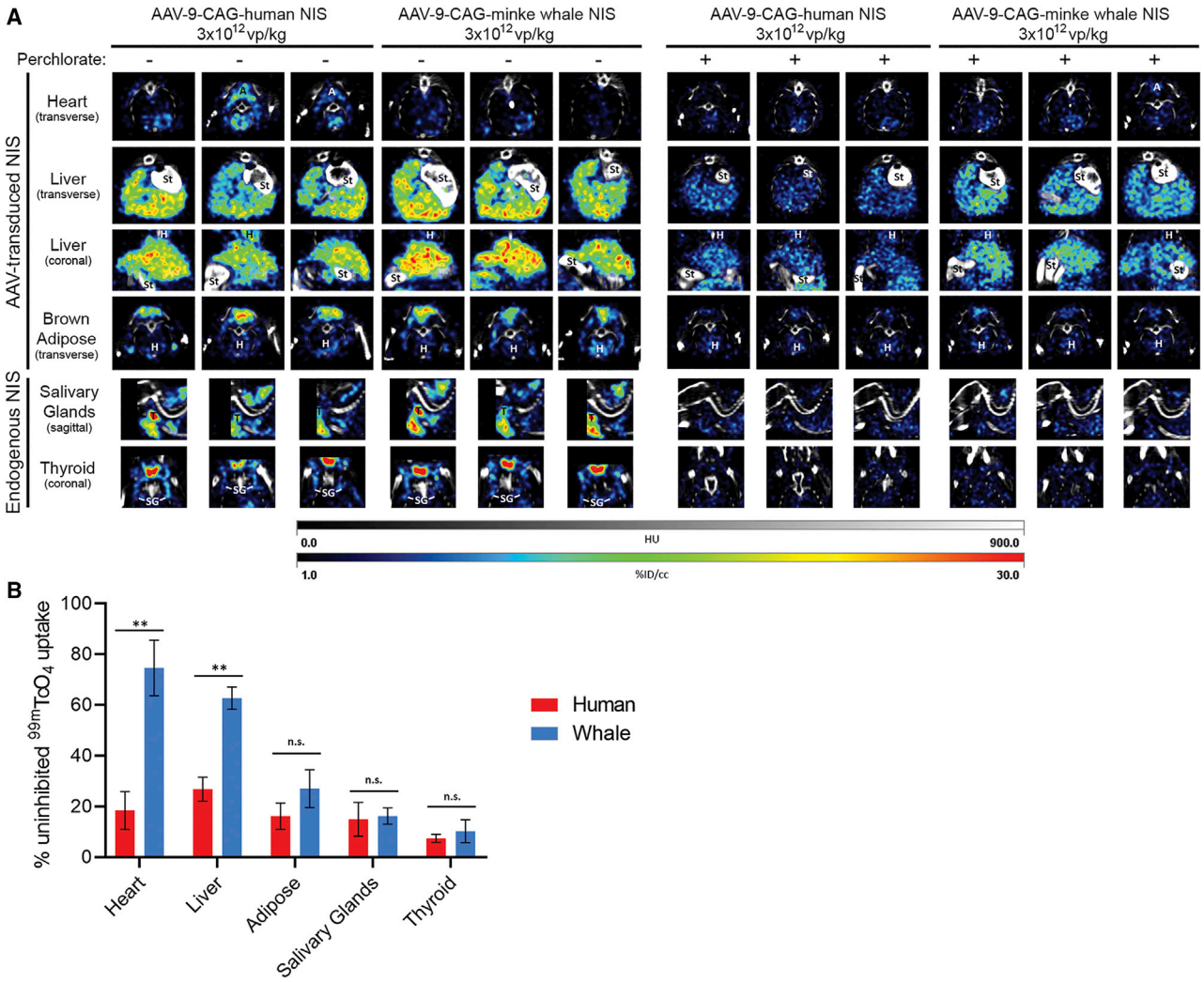

Figure 2. SPECT/CT with $^{99m}TcO_4$ and Perchlorate

(A) SPECT/CT slices in mice transduced with 3×10^{12} vp/kg AAV-9-CAG-human NIS or AAV-9-CAG-minke whale NIS imaged with $^{99m}TcO_4$ in the absence or presence of 100 μM blood concentration perchlorate. The brightest slices of each organ are represented for each of the three mice in both groups. Labels indicate organs in the imaging field that are not the focus of the slice. A, adipose; St, stomach and small intestine; H, heart; T, thyroid; SG, salivary gland; HU, Hounsfield units; %ID/cc, percent injected dose per cubic centimeter. (B) Quantification of signal intensity in (A) throughout entire organ. Values are shown as % uninhibited $^{99m}TcO_4$ uptake to normalize between mice. Note that the heart signal comparison is misleading due to the low initial signal observed with minke whale NIS. Error bars indicate SD. $^{**}p < 0.01$. n.s., not significant.

endogenous NIS-expressing tissues (salivary glands and thyroid) (Figure 2A). Animal-to-animal variability was observed, especially in imaging of the transduced heart tissue in both mice expressing hNIS or wNIS. Treatment with 100 μM perchlorate prior to $^{99m}TcO_4$ injection led to a significant decrease in radiotracer concentration in all tissues. There was a slight increase in the signal observed from the hearts and brown adipose tissue of AAV-9-CAG-wNIS-treated mice compared to AAV-9-CAG-hNIS-treated mice, but there was not enough signal retained with perchlorate pretreatment at this vector dose for practical *in vivo* imaging uses (Figure 2B). It is noteworthy that the heart signal comparison is misleading due to the low initial signal observed in mice treated with AAV-9-CAG-wNIS. The liver was the only tissue in which AAV-9-CAG-wNIS-treated mice retained significantly more radioisotope uptake compared to AAV-9-CAG-hNIS-treated mice. Pretreatment with perchlorate significantly reduced uptake in the salivary glands and thyroid in both groups.

PET/CT Imaging with $B^{18}F_4$ and Perchlorate

Mice treated with either 3×10^{12} vp/kg AAV-9-CAG-hNIS or AAV-9-CAG-wNIS were capable of concentrating $B^{18}F_4$ in both AAV-9-transduced tissues (heart, liver, and brown adipose) and in endogenous NIS-expressing tissues (salivary glands and thyroid) (Figure 3A). Animal-to-animal variability was observed but did not prevent

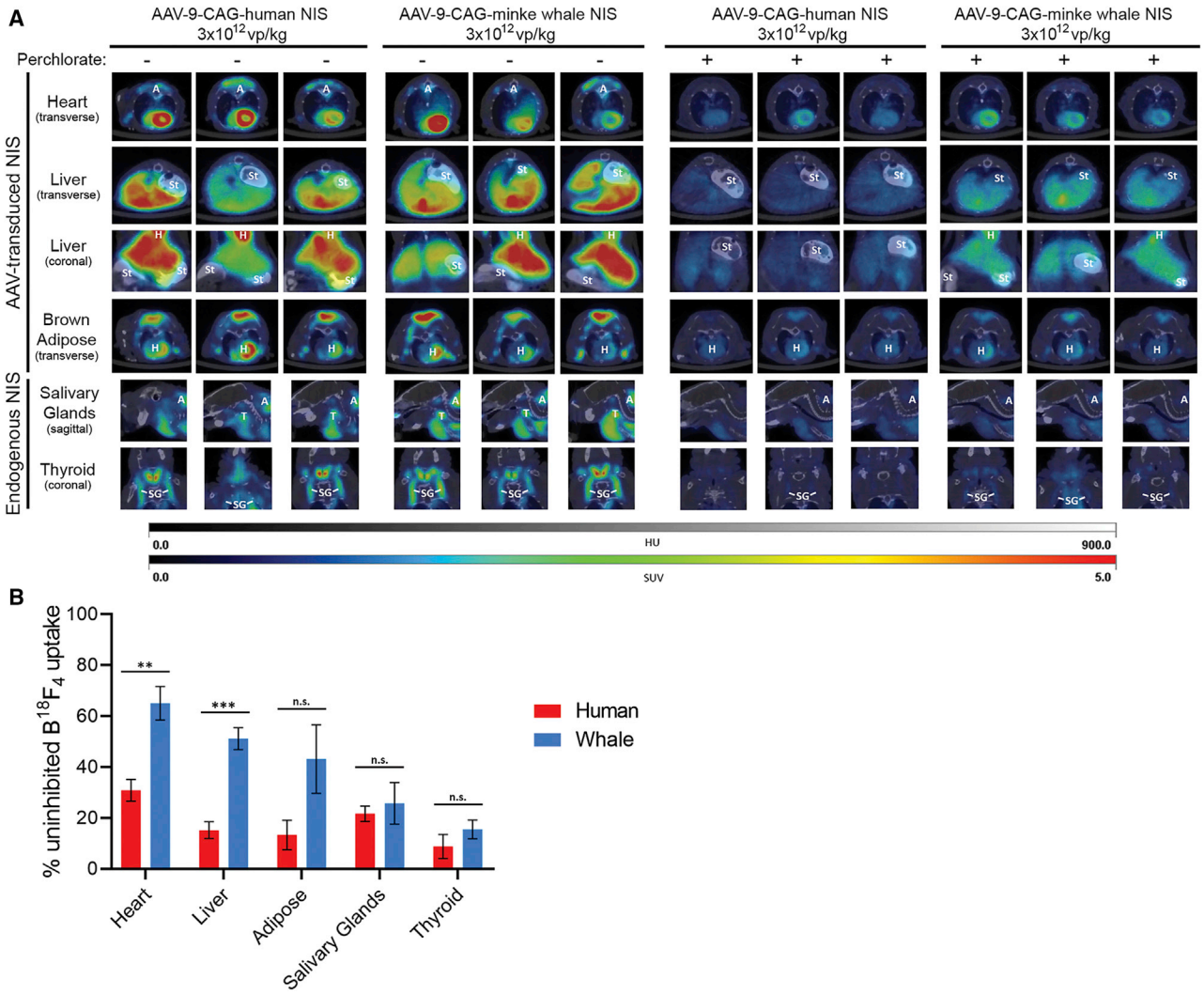

Figure 3. PET/CT with $B^{18}F_4$ and Perchlorate

(A) PET/CT slices in mice transduced with 3×10^{12} vp/kg AAV-9-CAG-human NIS or AAV-9-CAG-minke whale NIS imaged with $B^{18}F_4$ in the absence or presence of 100 μM blood concentration perchlorate. The brightest slices of each organ are represented for each of the three mice in both groups. Labels indicate organs in the imaging field that are not the focus of the slice. A, adipose; St, stomach and small intestine; H, heart; T, thyroid; SG, salivary gland. HU, Hounsfield units; SUV, standard uptake value. (B) Quantification of signal intensity in (A) throughout entire organ. Values are shown as % uninhibited $B^{18}F_4$ uptake to normalize between mice. Error bars indicate SD. $^{**}p < 0.01$, $^{***}p < 0.001$. n.s., not significant.

significant uptake in all target tissues. Treatment with 100 μM perchlorate prior to $B^{18}F_4$ injection led to a marked decrease in radiotracer concentration in all tissues. Appreciable signal was retained in the hearts, livers, and brown adipose tissue of AAV-9-CAG-wNIS-treated mice pretreated with perchlorate, although only the heart and liver were statistically significant. The loss of signal was more profound in AAV-9-CAG-hNIS-treated mice compared to AAV-9-CAG-wNIStreated mice (Figure 3B). $B^{18}F_4$ uptake was significantly reduced in the salivary and thyroid glands of both groups when pretreated with perchlorate. Three-dimensional reconstructions of the PET slices in mice treated with either AAV-9-CAG-hNIS or AAV-9-CAG-wNIS in the absence or presence of perchlorate reveal the extent of signal retention in mice expressing wNIS versus hNIS (Figure 4).

To test whether the administered dose of AAV-9-CAG-wNIS was a limiting factor in the signal observed, three mice were treated were with 1×10^{13} vp/kg AAV-9-CAG-wNIS and imaged in the absence and presence of perchlorate using $^{99m}TcO_4$ SPECT/CT (Figure S2) or $B^{18}F_4$ PET/CT (Figure S3). A significant increase in $^{99m}TcO_4$ and $B^{18}F_4$ uptake both with and without perchlorate was observed. $^{99m}TcO_4$ and perchlorate treatment in these mice revealed demonstrable signal retention in the heart, liver, and brown adipose while effectively reducing uptake by the salivary glands and thyroid

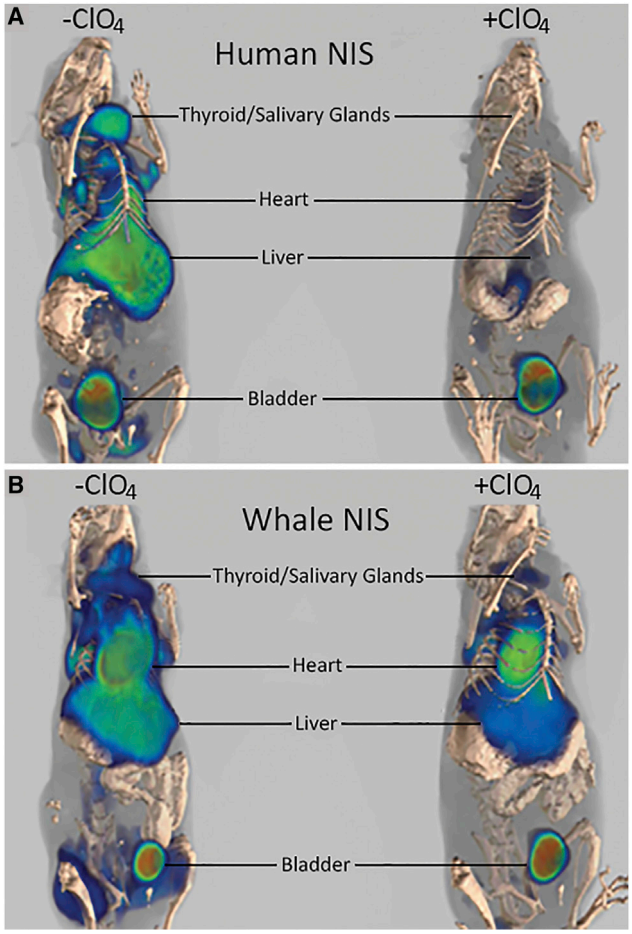

Figure 4. Three-Dimensional Reconstruction of B18F4 PET/CT of AAV-9-CAG-hNIS- or AAV-9-CAG-wNIS-Treated Mice in the Absence and Presence of Perchlorate

(A) AAV-9-CAG-hNIS-treated mice. (B) AAV-9-CAG-wNIS-treated mice. The first mouse from each representative column in Figure 3A is shown. Two of the AAV-9-transduced tissues, heart and liver, are indicated. Two major sites of endogenous uptake, the salivary glands and thyroid, are indicated. The bladder collects the radiotracers nonspecifically and is indicated.

(Figure S2). For $B^{18}F_4$, signal retention in the heart, liver, and adipose tissues was close to non-perchlorate pretreated levels (Figure S3). There was a reduction in $B^{18}F_4$ uptake in the salivary glands and thyroid, although inhibition of uptake in these tissues was not complete. This may be due to increased levels of $B^{18}F_4$ circulating in the blood as it leaks from heart, liver, or adipose tissue and is thus available for uptake as the temporary perchlorate inhibition subsides.

DISCUSSION

The utility of NIS for *in vivo* imaging via gamma scintigraphy, SPECT, and PET continues to expand to include applications such as the tracking of viral replication, virus spread, tumor response, tissue transduction, and cell trafficking. However, the full potential of NIS imaging remains unrealized due to several limitations, including uptake of radiotracers by endogenous NIS, radiotracer efflux, and limited *in vivo* expression in infected or transduced tissues. The most significant issue is endogenous NIS radiotracer uptake, which limits imaging resolution and precision. This study aimed to address the issue of endogenous NIS by using a perchlorate-resistant NIS variant for imaging and perchlorate inhibition to block endogenous NIS transport activity.

Our results show that the partial perchlorate resistance of wNIS observed *in vitro* also occurs *in vivo*. wNIS was more resistant to perchlorate inhibition than hNIS, permitting the testing of the application of perchlorate pretreatment for enhanced *in vivo* imaging. wNIS was able to concentrate more radiotracer into perchlorate-pretreated AAV-9-transduced tissues compared to hNIS. This effect was appreciable in the liver with $^{99m}TcO_4$ SPECT/CT imaging, and significant in the heart, liver, and adipose tissue with $B^{18}F_4$ PET/CT imaging. Additionally, perchlorate blockade led to a significant decrease of radiotracer uptake in naturally NIS-expressing tissues such as the thyroid and salivary glands of the mouse. There was some residual uptake with endogenous NIS in both the AAV-9-CAG-hNIS + perchlorate- and AAV-9-CAG-wNIS + perchlorate-treated mice. A higher dose of administered perchlorate may abolish this uptake, but this would also likely decrease the observed signal in transduced tissues. It may also not be possible to completely eliminate endogenous uptake, as some amount of radiotracer will continue to circulate as it effluxes from transduced tissues and may be captured by endogenous NIS. An increased dose of AAV-9-CAG-wNIS was able to improve the signal observed with perchlorate pretreatment for both $^{99m}TcO_4$ and $B^{18}F_4$ while reducing off-target uptake, suggesting that higher doses can be used for future studies to improve signal and safety.

The mechanism of perchlorate resistance in wNIS is currently unknown but is a subject of active investigation in our laboratory. Molecular modeling studies indicate the ion-binding sites of wNIS and hNIS are extremely similar and likely not the source of the observed differences.[49] We hypothesize that residue differences on the extracellular face of NIS are responsible for the increased perchlorate resistance of wNIS. A previous study identified several charged residues on the extracellular face of hNIS that affect the binding affinity (K_m) and transport velocity (V_{max}) of hNIS for iodide.[50] wNIS has additional charged residues in this region, suggesting wNIS may handle iodide, and by extension, perchlorate, differently than hNIS.[49] We are investigating the role of charged residues on the surface of wNIS as a mediator of its unique perchlorate resistance.

The inhibition of uptake by endogenous NIS may enable another promising application of NIS: radiovirotherapy. Despite impressive pre-clinical data supporting the combination of oncolytic viruses expressing NIS with ^{131}I or $^{188}ReO_4$ therapy in a variety of tumor types, this has not translated to clinical use.[15–19,38,44] A major limitation is off-target toxicity from ^{131}I, partially due to tissues that concentrate radioiodide, such as the thyroid and salivary glands, but also due to the myeloablative effect of beta radiation.[37–42,51] Use of perchlorate to block endogenous NIS would protect tissues that express NIS. It

would also reduce the dose necessary since endogenous NIS-expressing tissues would not act as a radiotracer sink. Further studies are required to test the efficacy of ^{131}I radiotherapy in combination with wNIS and perchlorate. This study presents a compelling use of an inhibitor-resistant NIS variant. The promising results observed in the present study prove that NIS biotechnology has more advances to make and more to offer regarding technological and clinical applications.

MATERIALS AND METHODS

NIS-Expressing Lentivirally Transduced HeLa Cells and Membrane-Localized NIS Quantification

Detailed methods for mammalian cell culture, NIS construct generation, lentiviral particle generation, stable cell line production, and characterization of extracellular membrane-localized NIS protein expression by flow cytometry used for this study were described previously.[49]

Perchlorate Dose-Response Assay

The same protocol described previously in Concilio et al.[49] was used for the perchlorate dose-response assay, except 1.5×10^5 HeLa-NIS cells were plated in six-well plates 3 days prior to the uptake assay. Two replicates of three wells were used for each condition. Immediately prior to the uptake assay, cells were incubated at 37°C in 1 mL of uptake buffer (Hanks' balanced salt solution [HBSS] + 10 mM HEPES [pH 7.4]) with or without the indicated concentration of potassium perchlorate.

Recombinant AAV-9 Vector Production

AAV vectors were generated by packaging AAV-2-based recombinant genomes in AAV-9 capsids. The production of these pseudotyped AAV-2/9 vectors (AAV-9) was performed by triple transfection using an adenovirus-free system (Agilent Technologies, Santa Clara, CA, USA). Briefly, HEK293T cells were transfected in 15-cm plates using linear polyethylenimine at an N/P ratio of 22 (L-PEI max 25 kDa, Polysciences, Warrington, PA, USA) and a 50-μg equimolar mixture of the three following plasmids per plate: the *trans*-complementing adenovirus helper plasmid pHelper (Agilent Technologies), the pRep2Cap9 packaging plasmid expressing the AAV-2 rep gene and the AAV-9 cap gene (kindly provided by James M. Wilson, University of Pennsylvania, PA, USA), and a *cis*-acting AAV vector plasmid (pAAV-CAG-hNIS or pAAV-CAG-wNIS). After 72 h of transfection, the collected cells underwent three cycles of freeze/thaw; the crude lysate was then clarified at 13,400 × *g* for 20 min at 4°C. The supernatant obtained was resolved by ultracentrifugation at ~400,000 × *g* for 2 h at 4°C over a discontinuous iodixanol gradient (OptiPrep, Sigma, St. Louis, MO, USA) as described by Lock et al.[52] and iodixanol fractions of density 40%–54% interface were collected, desalted, and concentrated in sterile PBS using centrifugal filter devices (Amicon Ultra-15 molecular weight cutoff [MWCO] 100K, Millipore). Vector stocks were titrated using quantitative real-time PCR against a standard linear plasmid range by amplifying the human growth hormone polyadenylation signal with forward primer 5′-CCTGGGTTCAAGCGATTCTC-3′, reverse primer 5′-AGCT GAGCCTGGTCATGCAT-3′, and hydrolysis probe 5′-TGCCT CAGCCTCCCGAGTTGTTG-3′.

Animals and AAV-9 Vector Administrations

This study was approved by the Mayo Institutional Animal Care and Use Committee and conducted in accordance with the NIH *Guidelines for the Care and Use of Laboratory Animals* (Institutional Animal Care and Use Committee [IACUC] #A21815). Athymic male mice were injected with AAV-9 intravenously through the tail vein. The administration dose was 3×10^{12} vp/kg. Imaging started 14 days after AAV-9 administration.

SPECT Imaging

Mice were injected with 300 μCi of $^{99m}TcO_4$ via the tail vein 1 h prior to image acquisition. Imaging was performed in the Mayo Clinic Small Animal Imaging Core Facility using a U-SPECT-II/CT scanner (MILabs, Utrecht, the Netherlands). Scan volumes for both SPECT and CT were selected based on orthogonal optical images provided by integrated webcams. Micro-CT image acquisition was performed in 4 min, for normal resolution (169-μm square voxels, 640 slices) at 0.5 mA and 60 kV. Image acquisition time was approximately 20 min for SPECT (69 projections at 50 s per bed position). All pinholes focused on a single volume in the center of the tube; by using an XYZ stage, large volumes up to the entire animal were scanned at uniform resolution. Co-registration of the SPECT and CT images was performed by applying pre-calibrated spatial transformation to the SPECT images to match with the CT images. SPECT reconstruction was performed using a POSEM (pixel-based ordered subset expectation maximization) algorithm with six iterations and 16 subsets. CT data were reconstructed using a Feldkamp cone beam algorithm (NRecon v1.6.3, Skyscan). After reconstruction, SPECT images were automatically registered to the CT images according to the pre-calibrated transformation, and re-sampled to the CT voxel size. Co-registered images were further rendered and visualized using PMOD software version 3.504. A three-dimensional Gaussian filter (0.8 mm full width at half maximum [FWHM]) was applied to suppress noise, and lookup tables (LUTs) were adjusted for good visual contrast. Reconstructed images were visualized as both orthogonal slices and maximum intensity projections. Maximal intensity projection videos and three-dimensional rendering of regions of interests were performed using PMOD software version 3.504.

PET Imaging

For PET imaging, mice received 300 μCi of $B^{18}F_4$ 45 min prior to image acquisition. PET/CT imaging was performed on a small animal Inveon multiple modality PET/CT scanner (Siemens). CT was performed at 80 kEv, 500 μA, with 250 ms/projection, 180 projections, and bin 4; the effective pixel size was 94.59 μm. PET was performed using 10-min acquisition, OSEM2D reconstruction with Fourier rebinning, and four iterations. Co-registered images were rendered and visualized using the PMOD software version 3.504.

Barium Sulfate Gavage and *In Vivo* Perchlorate Inhibition

In order to distinguish between radiotracer signals from endogenous NIS expression in stomach mucosa and AAV-9-transduced NIS in the liver, 350 μL of barium sulfate contrast was given via oral gavage before image acquisition in both SPECT and PET imaging. In the imaging studies where perchlorate inhibition was tested, mice were pretreated intraperitoneally with $NaClO_4$ at the indicated concentration 30 min before radiotracer administration.

Software and Statistics

Flow cytometry data were analyzed using FlowJo 10. Figures and statistics were generated using GraphPad Prism 8.1.1 and Photoshop CC. The graphical abstract was generated using BioRender. IC_{50} values were calculated via non-linear regression using the equation setting: (inhibitor) versus normalized response — variable slope — inhibition. p values for Figures 2 and 3 were calculated using an unpaired t test with the two-stage linear step-up procedure of Benjamini, Krieger, and Yekutieli, with Q = 1% as suggested by Prism 8.1.1. Each row was analyzed individually, without assuming a consistent SD. SPECT/CT and PET/CT images were captured and analyzed using PMOD software version 3.504. Images were normalized to radiation dose at the time of image analysis.

SUPPLEMENTAL INFORMATION

Supplemental Information can be found online at https://doi.org/10.1016/j.ymthe.2020.09.036.

AUTHOR CONTRIBUTIONS

S.C.C. performed the *in vitro* experiments, analyzed the imaging data, and wrote the manuscript. L.S. designed and performed the *in vivo* imaging experiments. L.P. cloned, generated, and titered the AAV-9 viruses. K.-W.P. and S.J.R. provided guidance, funding, and manuscript reviews. All authors reviewed and approved the manuscript.

CONFLICTS OF INTEREST

S.J.R. and K.-W.P. are cofounders of and hold equity in Imanis Life Sciences, a reporter gene imaging company. L.S. is a current employee of Imanis Life Sciences. The use of minke whale NIS for *in vivo* animal imaging of gene therapy and oncolytic virotherapy has been submitted as an invention disclosure to Mayo Clinic Ventures. S.C.C., S.J.R., K.-W.P., and L.S. are listed as co-inventors. L.P. declares no competing interests.

ACKNOWLEDGMENTS

We thank Tracy Decklever and Cynthia Vernon with the Mayo Clinic Nuclear Imaging Facility for vital assistance with the animal imaging experiments. This study was supported by National Institutes of Health grants R44 TR001191 (to S.J.R.) and T32 AI132165 01A1 (to S.C.C.).

REFERENCES

1. Kotani, T., Ogata, Y., Yamamoto, I., Aratake, Y., Kawano, J.I., Suganuma, T., and Ohtaki, S. (1998). Characterization of gastric Na^+/I^- symporter of the rat. Clin. Immunol. Immunopathol. *89*, 271–278.
2. Nicola, J.P., Basquin, C., Portulano, C., Reyna-Neyra, A., Paroder, M., and Carrasco, N. (2009). The Na^+/I^- symporter mediates active iodide uptake in the intestine. Am. J. Physiol. Cell Physiol. *296*, C654–C662.
3. Spitzweg, C., Joba, W., Eisenmenger, W., and Heufelder, A.E. (1998). Analysis of human sodium iodide symporter gene expression in extrathyroidal tissues and cloning of its complementary deoxyribonucleic acids from salivary gland, mammary gland, and gastric mucosa. J. Clin. Endocrinol. Metab. *83*, 1746–1751.
4. Spitzweg, C., Dutton, C.M., Castro, M.R., Bergert, E.R., Goellner, J.R., Heufelder, A.E., and Morris, J.C. (2001). Expression of the sodium iodide symporter in human kidney. Kidney Int. *59*, 1013–1023.
5. Riesco-Eizaguirre, G., Leoni, S.G., Mendiola, M., Estevez-Cebrero, M.A., Gallego, M.I., Redondo, A., Hardisson, D., Santisteban, P., and De la Vieja, A. (2014). NIS mediates iodide uptake in the female reproductive tract and is a poor prognostic factor in ovarian cancer. J. Clin. Endocrinol. Metab. *99*, E1199–E1208.
6. Russo, D., Scipioni, A., Durante, C., Ferretti, E., Gandini, L., Maggisano, V., Paoli, D., Verrienti, A., Costante, G., Lenzi, A., and Filetti, S. (2011). Expression and localization of the sodium/iodide symporter (NIS) in testicular cells. Endocrine *40*, 35–40.
7. Ullberg, S., and Ewaldsson, B. (1964). Distribution of radio-iodine studied by whole-body autoradiography. Acta Radiol. Ther. Phys. Biol. *2*, 24–32.
8. Chung, T., Youn, H., Yeom, C.J., Kang, K.W., and Chung, J.K. (2015). Glycosylation of sodium/iodide symporter (NIS) regulates its membrane translocation and radioiodine uptake. PLoS ONE *10*, e0142984.
9. Huc-Brandt, S., Marcellin, D., Graslin, F., Averseng, O., Bellanger, L., Hivin, P., Quemeneur, E., Basquin, C., Navarro, V., Pourcher, T., and Darrouzet, E. (2011). Characterisation of the purified human sodium/iodide symporter reveals that the protein is mainly present in a dimeric form and permits the detailed study of a native C-terminal fragment. Biochim. Biophys. Acta *1808*, 65–77.
10. Levy, O., Dai, G., Riedel, C., Ginter, C.S., Paul, E.M., Lebowitz, A.N., and Carrasco, N. (1997). Characterization of the thyroid Na^+/I^- symporter with an anti-COOH terminus antibody. Proc. Natl. Acad. Sci. USA *94*, 5568–5573.
11. Levy, O., De la Vieja, A., Ginter, C.S., Riedel, C., Dai, G., and Carrasco, N. (1998). N-linked glycosylation of the thyroid Na^+/I^- symporter (NIS). Implications for its secondary structure model. J. Biol. Chem. *273*, 22657–22663.
12. Wolff, J., and Maurey, J.R. (1963). Thyroidal iodide transport. IV. The role of ion size. Biochim. Biophys. Acta *69*, 58–67.
13. Van Sande, J., Massart, C., Beauwens, R., Schoutens, A., Costagliola, S., Dumont, J.E., and Wolff, J. (2003). Anion selectivity by the sodium iodide symporter. Endocrinology *144*, 247–252.
14. Miller, A., and Russell, S.J. (2016). The use of the NIS reporter gene for optimizing oncolytic virotherapy. Expert Opin. Biol. Ther. *16*, 15–32.
15. Hutzen, B., Pierson, C.R., Russell, S.J., Galanis, E., Raffel, C., and Studebaker, A.W. (2012). Treatment of medulloblastoma using an oncolytic measles virus encoding the thyroidal sodium iodide symporter shows enhanced efficacy with radioiodine. BMC Cancer *12*, 508.
16. Riese, C.G., Seitz, S., Schipper, M.L., and Behr, T.M. (2009). Effective treatment of pancreatic neuroendocrine tumours transfected with the sodium iodide symporter gene by ^{186}Re-perrhenate in mice. Eur. J. Nucl. Med. Mol. Imaging *36*, 1767–1773.
17. Dadachova, E., Nguyen, A., Lin, E.Y., Gnatovskiy, L., Lu, P., and Pollard, J.W. (2005). Treatment with rhenium-188-perrhenate and iodine-131 of NIS-expressing mammary cancer in a mouse model remarkably inhibited tumor growth. Nucl. Med. Biol. *32*, 695–700.
18. Petrich, T., Helmeke, H.J., Meyer, G.J., Knapp, W.H., and Pötter, E. (2002). Establishment of radioactive astatine and iodine uptake in cancer cell lines expressing the human sodium/iodide symporter. Eur. J. Nucl. Med. Mol. Imaging *29*, 842–854.
19. Shimura, H., Haraguchi, K., Miyazaki, A., Endo, T., and Onaya, T. (1997). Iodide uptake and experimental ^{131}I therapy in transplanted undifferentiated thyroid cancer cells expressing the Na^+/I^- symporter gene. Endocrinology *138*, 4493–4496.
20. Miyagawa, M., Beyer, M., Wagner, B., Anton, M., Spitzweg, C., Gansbacher, B., Schwaiger, M., and Bengel, F.M. (2005). Cardiac reporter gene imaging using the human sodium/iodide symporter gene. Cardiovasc. Res. *65*, 195–202.
21. Barton, K.N., Xia, X., Yan, H., Stricker, H., Heisey, G., Yin, F.F., Nagaraja, T.N., Zhu, G., Kolozsvary, A., Fenstermacher, J.D., et al. (2004). A quantitative method for

measuring gene expression magnitude and volume delivered by gene therapy vectors. Mol. Ther. *9*, 625–631.

22. Russell, S.J., Federspiel, M.J., Peng, K.W., Tong, C., Dingli, D., Morice, W.G., Lowe, V., O'Connor, M.K., Kyle, R.A., Leung, N., et al. (2014). Remission of disseminated cancer after systemic oncolytic virotherapy. Mayo Clin. Proc. *89*, 926–933.
23. Moulay, G., Ohtani, T., Ogut, O., Guenzel, A., Behfar, A., Zakeri, R., Haines, P., Storlie, J., Bowen, L., Pham, L., et al. (2015). Cardiac AAV9 gene delivery strategies in adult canines: assessment by long-term serial SPECT imaging of sodium iodide symporter expression. Mol. Ther. *23*, 1211–1221.
24. Penheiter, A.R., Russell, S.J., and Carlson, S.K. (2012). The sodium iodide symporter (NIS) as an imaging reporter for gene, viral, and cell-based therapies. Curr. Gene Ther. *12*, 33–47.
25. Bishnoi, S., Tiwari, R., Gupta, S., Byrareddy, S.N., and Nayak, D. (2018). Oncotargeting by vesicular stomatitis virus (VSV): advances in cancer therapy. Viruses *10*, 90.
26. Niu, G., Krager, K.J., Graham, M.M., Hichwa, R.D., and Domann, F.E. (2005). Noninvasive radiological imaging of pulmonary gene transfer and expression using the human sodium iodide symporter. Eur. J. Nucl. Med. Mol. Imaging *32*, 534–540.
27. Terrovitis, J., Kwok, K.F., Lautamäki, R., Engles, J.M., Barth, A.S., Kizana, E., Miake, J., Leppo, M.K., Fox, J., Seidel, J., et al. (2008). Ectopic expression of the sodium-iodide symporter enables imaging of transplanted cardiac stem cells in vivo by single-photon emission computed tomography or positron emission tomography. J. Am. Coll. Cardiol. *52*, 1652–1660.
28. Lehner, S., Lang, C., Kaissis, G., Todica, A., Zacherl, M.J., Boening, G., Spitzweg, C., Herbach, N., Franz, W.M., Krause, B.J., et al. (2015). ^{124}I-PET assessment of human sodium iodide symporter reporter gene activity for highly sensitive in vivo monitoring of teratoma formation in mice. Mol. Imaging Biol. *17*, 874–883.
29. Seo, J.H., Jeon, Y.H., Lee, Y.J., Yoon, G.S., Won, D.I., Ha, J.H., Jeong, S.Y., Lee, S.W., Ahn, B.C., and Lee, J. (2010). Trafficking macrophage migration using reporter gene imaging with human sodium iodide symporter in animal models of inflammation. J. Nucl. Med. *51*, 1637–1643.
30. Sharif-Paghaleh, E., Sunassee, K., Tavaré, R., Ratnasothy, K., Koers, A., Ali, N., Alhabbab, R., Blower, P.J., Lechler, R.I., Smyth, L.A., et al. (2011). In vivo SPECT reporter gene imaging of regulatory T cells. PLoS ONE *6*, e25857.
31. Hickey, R.D., Mao, S.A., Glorioso, J., Elgilani, F., Amiot, B., Chen, H., Rinaldo, P., Marler, R., Jiang, H., DeGrado, T.R., et al. (2016). Curative ex vivo liver-directed gene therapy in a pig model of hereditary tyrosinemia type 1. Sci. Transl. Med. *8*, 349ra99.
32. Dwyer, R.M., Ryan, J., Havelin, R.J., Morris, J.C., Miller, B.W., Liu, Z., Flavin, R., O'Flatharta, C., Foley, M.J., Barrett, H.H., et al. (2011). Mesenchymal stem cell-mediated delivery of the sodium iodide symporter supports radionuclide imaging and treatment of breast cancer. Stem Cells *29*, 1149–1157.
33. Shi, S., Zhang, M., Guo, R., Miao, Y., Zhang, M., Hu, J., Xi, Y., and Li, B. (2014). Feasibility of lentiviral-mediated sodium iodide symporter gene delivery for the efficient monitoring of bone marrow-derived mesenchymal stem cell transplantation and survival. Int. J. Mol. Med. *34*, 1547–1554.
34. Müller, A.M., Schmohl, K.A., Knoop, K., Schug, C., Urnauer, S., Hagenhoff, A., Clevert, D.A., Ingrisch, M., Niess, H., Carlsen, J., et al. (2016). Hypoxia-targeted ^{131}I therapy of hepatocellular cancer after systemic mesenchymal stem cell-mediated sodium iodide symporter gene delivery. Oncotarget *7*, 54795–54810.
35. Shi, S., Zhang, M., Guo, R., Miao, Y., and Li, B. (2019). Bone marrow-derived mesenchymal stem cell-mediated dual-gene therapy for glioblastoma. Hum. Gene Ther. *30*, 106–117.
36. Tutter, M., Schug, C., Schmohl, K.A., Urnauer, S., Schwenk, N., Petrini, M., Lokerse, W.J.M., Zach, C., Ziegler, S., Bartenstein, P., et al. (2020). Effective control of tumor growth through spatial and temporal control of theranostic sodium iodide symporter (*NIS*) gene expression using a heat-inducible gene promoter in engineered mesenchymal stem cells. Theranostics *10*, 4490–4506.
37. Ahn, B.C. (2012). Sodium iodide symporter for nuclear molecular imaging and gene therapy: from bedside to bench and back. Theranostics *2*, 392–402.
38. Opyrchal, M., Allen, C., Iankov, I., Aderca, I., Schroeder, M., Sarkaria, J., and Galanis, E. (2012). Effective radiovirotherapy for malignant gliomas by using oncolytic measles virus strains encoding the sodium iodide symporter (MV-NIS). Hum. Gene Ther. *23*, 419–427.
39. Sioka, C., and Fotopoulos, A. (2011). Effects of I-131 therapy on gonads and pregnancy outcome in patients with thyroid cancer. Fertil. Steril. *95*, 1552–1559.
40. Klein Hesselink, E.N., Brouwers, A.H., de Jong, J.R., van der Horst-Schrivers, A.N., Coppes, R.P., Lefrandt, J.D., Jager, P.L., Vissink, A., and Links, T.P. (2016). Effects of radioiodine treatment on salivary gland function in patients with differentiated thyroid carcinoma: a prospective study. J. Nucl. Med. *57*, 1685–1691.
41. Selvakumar, T., Nies, M., Klein Hesselink, M.S., Brouwers, A.H., van der Horst-Schrivers, A.N.A., Klein Hesselink, E.N., Tissing, W.J.E., Vissink, A., Links, T.P., Bocca, G., et al. (2018). Long-term effects of radioiodine treatment on salivary gland function in adult survivors of pediatric differentiated thyroid carcinoma. J. Nucl. Med. *60*, 172–177.
42. Morgenstern, K.E., Vadysirisack, D.D., Zhang, Z., Cahill, K.V., Foster, J.A., Burns, J.A., Kloos, R.T., and Jhiang, S.M. (2005). Expression of sodium iodide symporter in the lacrimal drainage system: implication for the mechanism underlying nasolacrimal duct obstruction in I^{131}-treated patients. Ophthal. Plast. Reconstr. Surg. *21*, 337–344.
43. Kitahara, C.M., Berrington de Gonzalez, A., Bouville, A., Brill, A.B., Doody, M.M., Melo, D.R., Simon, S.L., Sosa, J.A., Tulchinsky, M., Villoing, D., and Preston, D.L. (2019). Association of radioactive iodine treatment with cancer mortality in patients with hyperthyroidism. JAMA Intern. Med. *179*, 1034–1042.
44. Mitrofanova, E., Unfer, R., Vahanian, N., and Link, C. (2006). Rat sodium iodide symporter allows using lower dose of ^{131}I for cancer therapy. Gene Ther. *13*, 1052–1056.
45. Hu, S., Cao, W., Lan, X., He, Y., Lang, J., Li, C., Hu, J., An, R., Gao, Z., and Zhang, Y. (2011). Comparison of rNIS and hNIS as reporter genes for noninvasive imaging of bone mesenchymal stem cells transplanted into infarcted rat myocardium. Mol. Imaging *10*, 227–237.
46. Suksanpaisan, L., Pham, L., McIvor, S., Russell, S.J., and Peng, K.W. (2013). Oral contrast enhances the resolution of in-life NIS reporter gene imaging. Cancer Gene Ther. *20*, 638–641.
47. Kim, Y.H., Youn, H., Na, J., Hong, K.J., Kang, K.W., Lee, D.S., and Chung, J.K. (2015). Codon-optimized human sodium iodide symporter (opt-hNIS) as a sensitive reporter and efficient therapeutic gene. Theranostics *5*, 86–96.
48. Jiang, H., and DeGrado, T.R. (2018). [^{18}F]tetrafluoroborate ([^{18}F]TFB) and its analogs for PET imaging of the sodium/iodide symporter. Theranostics *8*, 3918–3931.
49. Concilio, S.C., Zhekova, H.R., Noskov, S.Y., and Russell, S.J. (2020). Inter-species variation in monovalent anion substrate selectivity and inhibitor sensitivity in the sodium iodide symporter (NIS). PLoS ONE *15*, e0229085.
50. Li, C.C., Ho, T.Y., Kao, C.H., Wu, S.L., Liang, J.A., and Hsiang, C.Y. (2010). Conserved charged amino acid residues in the extracellular region of sodium/iodide symporter are critical for iodide transport activity. J. Biomed. Sci. *17*, 89.
51. Buchmann, I., Meyer, R.G., Mier, W., and Haberkorn, U. (2009). Myeloablative radioimmunotherapy in conditioning prior to haematological stem cell transplantation: closing the gap between benefit and toxicity? Eur. J. Nucl. Med. Mol. Imaging *36*, 484–498.
52. Lock, M., Alvira, M., Vandenberghe, L., Samanta, A., Toelen, J., Debyser, Z., et al. (2010). Rapid, Simple, and Versatile Manufacturing of Recombinant Adeno-Associated Viral Vectors at Scale. Hum. Gene Ther. *21*, 1259–1271.

YMTHE, Volume *29*

Supplemental Information

Improved Noninvasive *In Vivo* Tracking of AAV-9 Gene Therapy Using the Perchlorate-Resistant Sodium Iodide Symporter from Minke Whale

Susanna C. Concilio, Lukkana Suksanpaisan, Linh Pham, Kah-Whye Peng, and Stephen J. Russell

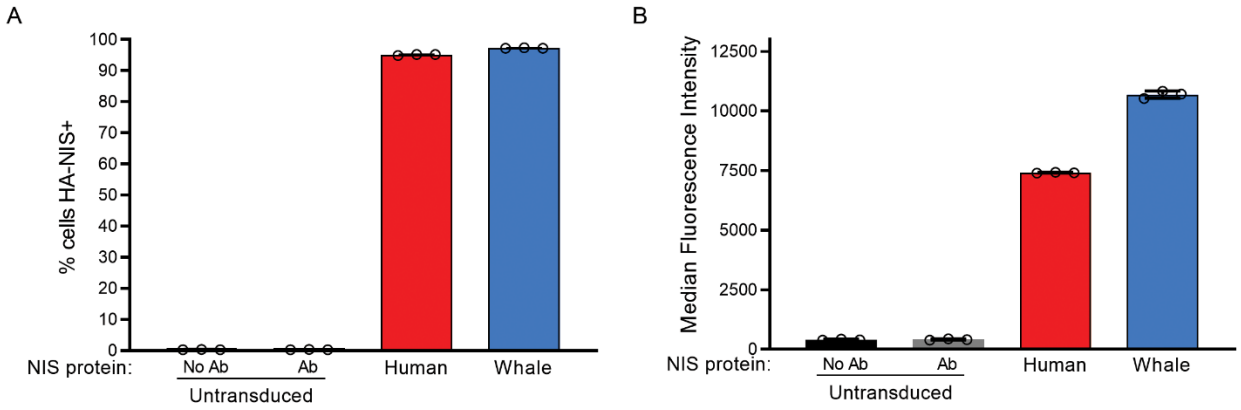

Figure S1. Flow cytometry characterization of lentivirally-transduced HeLa cells expressing HA-human NIS and HA-minke whale NIS. A) Percentage of puromycin selected lentivirally-transduced HeLa cells positively stained with α-HA-AlexaFluor647 antibody. B) Mean fluorescence intensity of puromycin selected lentivirally-transduced HeLa cells stained with α-HA-AlexaFluor647 antibody.

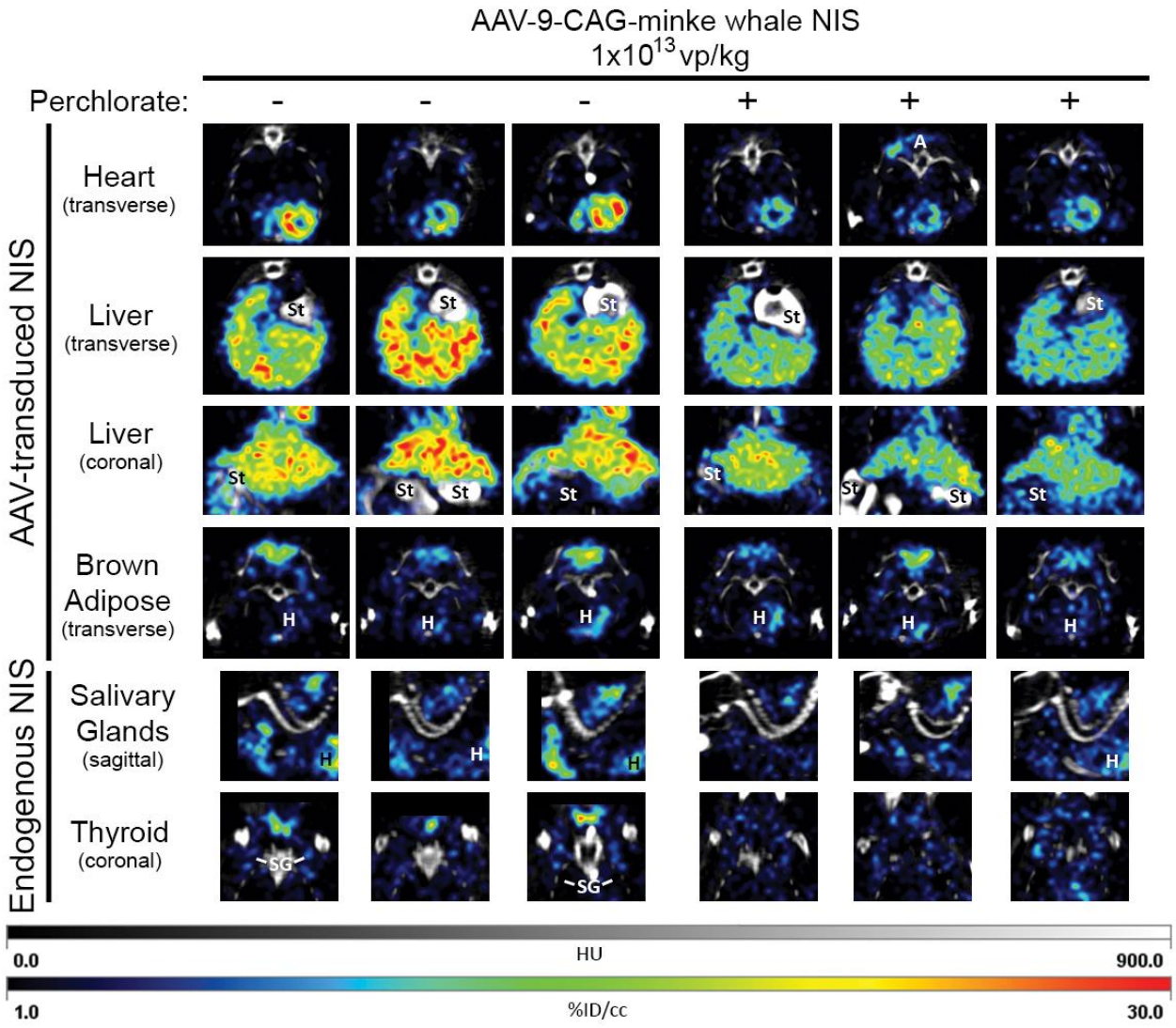

Figure S2. SPECT/CT with $^{99m}TcO_4$ with high dose AAV-9-CAG-minke whale NIS and perchlorate. SPECT/CT slices in mice transduced with $1x10^{13}$ vp/kg AAV-9-CAG-human NIS or AAV-9-CAG-minke whale NIS imaged with $^{99m}TcO_4$ in the absence or presence of 100 µM blood concentration perchlorate. The brightest slices of each organ are represented for each of the three mice in both groups. Labels indicate organs in the imaging field which are not the focus of the slice; A = adipose; St = stomach and small intestine; H = heart; T = thyroid; SG = salivary glands. HU = Hounsfield units; %ID/cc = percent injected dose per cubic centimeter.

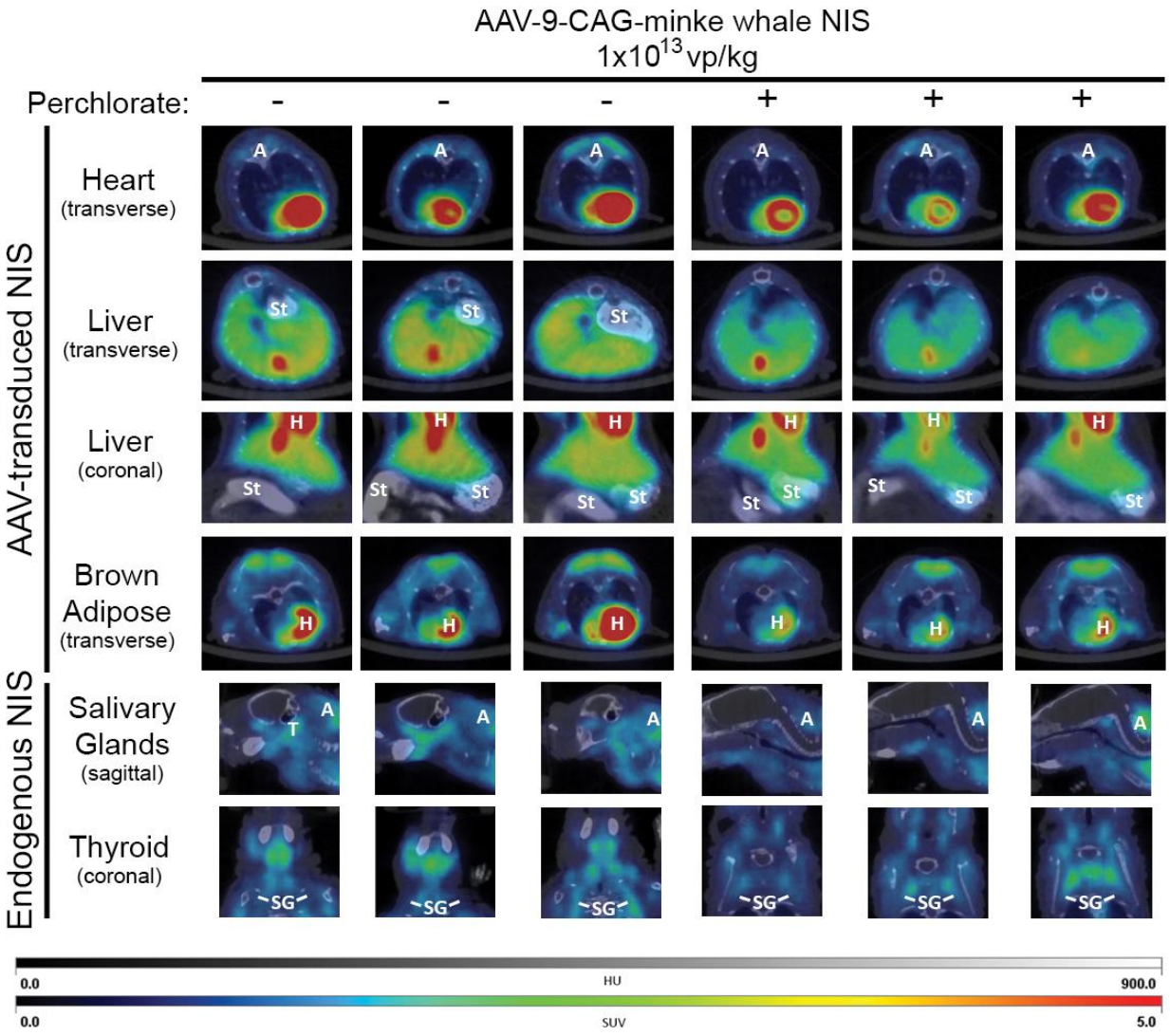

Figure S3. PET/CT with $B^{18}F_4$ with high dose AAV-9-CAG-minke whale NIS and perchlorate. PET/CT slices in mice transduced with $1x10^{13}$ vp/kg AAV-9-CAG-minke whale NIS imaged with $B^{18}F_4$ in the absence or presence of 100 µM blood concentration perchlorate. The brightest slices of each organ are represented for each of the three mice. Labels indicate organs in the imaging field which are not the focus of the slice; A = adipose; St = stomach and small intestine; H = heart; T = thyroid; SG = salivary glands. HU = Hounsfield units; SUV = standardized uptake value.